

# Progress in Organic Photodiodes through Physical Process Insights

Hrisheekesh Thachoth Chandran, Cenqi Yan, and Gang Li\*

Photodetectors based on organic materials have enormous potential due to their attractive optoelectronic and mechanical properties. In recent years, some of the performance metrics comparable to the conventional inorganic photodetectors have been realized in visible-range organic photodiodes (OPDs). These advancements in OPDs are mainly driven by innovations in device engineering and material design. However, insights into the fundamental performance limiting factors are imperative to further understand, optimize, and predict the performance metrics of OPD devices beyond conventional wisdom. In this review, the major progress in understandings related to trap state, charge transfer state, and noise/detectivity limits in OPD devices are highlighted.

## 1. Introduction

Photodetectors are vital components in applications like health monitoring,<sup>[1]</sup> optical communication,<sup>[2]</sup> night vision,<sup>[3]</sup> surveillance,<sup>[4]</sup> motion detection,<sup>[5]</sup> collision avoidance systems for autonomous vehicles, etc.<sup>[6,7]</sup> Due to their mature fabrication technology, appreciable performance, robust stability, and high-level integration with existing electronics, crystalline inorganic semiconductors-based photodetectors remain the choice of photodetection technology.<sup>[8,9]</sup> However, these inorganic photodetectors (IPDs) are facing challenges in fitting into the new age flexible/wearable devices due to their rigid/brittle nature.<sup>[10]</sup> The expensive and complicated manufacturing of IPD is also causing issues in realizing low-cost mass production. Being broadband absorbers, the use of color filters is a prerequisite in IPD for narrowband sensing.<sup>[11–13]</sup> Integration of color filters further complicates the device architecture and negatively affects pure color replication. Thus, scientific communities are in search of potential IPD


alternatives that offer low-cost fabrication, high performance, stability, and favorable mechanical properties.

Solution-processed photodetectors are potential alternatives to IPDs, primarily due to low-cost fabrication and attractive mechanical properties.<sup>[14–16]</sup> Photodetectors that can adhere to flexible, curved, and soft surfaces are in high demand due to their applications in human-activity monitoring and personal health care.<sup>[17–19]</sup> Organic photodetectors are the front runners in this segment and offer enormous advantages like tunable optoelectronic properties,<sup>[20]</sup> low-temperature/low-cost processing,<sup>[21]</sup> flexibility,<sup>[19]</sup> lightweight,<sup>[22]</sup> and biocompat-

ibility.<sup>[23]</sup> Two terminal organic PDs have either photoconductor or photodiode architecture.<sup>[20]</sup> For photoconductors, organic semiconductor is sandwiched between two symmetrical contacts. Due to the carrier recirculation through symmetrical contacts, this device structure allows photoconductive gain  $>100\%$ .<sup>[20]</sup> Photomultiplier (PM)-type organic photodetector with charge tunneling injection is also capable of producing gain. Recent efforts have realized novel broadband/narrowband PM-type organic photodetectors with an external quantum efficiency (EQE) values much higher than 100%.<sup>[24–29]</sup> However, as a result of carrier trapping, the response speed of PM organic photodetectors is relatively slow.<sup>[20]</sup> Depending upon the application, a compromise between gain and response speed is indeed needed.<sup>[30]</sup>

The most common type of organic photodetector is an organic photodiode (OPD). A photodiode has a simple architecture in which an active layer is sandwiched between transparent and metal electrodes.<sup>[6,20,31]</sup> The structure and working principle are more like organic solar cells.<sup>[6]</sup> Though the photodiodes do not produce any gain effect, they exhibit low dark current density ( $J_d$ ), fast temporal response, and broad linear dynamic (LDR) range.<sup>[6]</sup> Intense research efforts in the past few years have transformed OPD with some of the figure of merits (FOMs) comparable to IPD in the visible range.<sup>[32]</sup> Advances in broadband and narrowband OPDs are typically achieved by novel material design strategies and device/interface engineering.<sup>[33–36]</sup> OPDs were demonstrated with attractive FOMs like low  $J_d$ ,<sup>[32]</sup> high responsivity ( $R$ ) approaching  $0.5 \text{ A W}^{-1}$ ,<sup>[37]</sup> specific detectivity ( $D^*$ ) in the order of  $10^{12}$  (from direct experimental noise-characteristics)/ $10^{13}$  (shot-noise limited) Jones,<sup>[32,38]</sup> LDR over 8 orders and temporal response in the sub-microsecond range.<sup>[37,39]</sup> Narrowband OPDs were realized with ultralow full width half maximum (FWHM) values using novel device concepts like charge collection narrowing (CCN) and exciton dissociation narrowing (EDN).<sup>[33,34]</sup> Introduction of new active layer

H. Thachoth Chandran, C. Yan, G. Li  
Department of Electronic and Information Engineering, Research Institute for Smart Energy (RISE)  
The Hong Kong Polytechnic University  
Hung Hom, Kowloon, Hong Kong SAR, P. R. China  
E-mail: gang.w.li@polyu.edu.hk

 The ORCID identification number(s) for the author(s) of this article can be found under <https://doi.org/10.1002/aesr.202200002>.

© 2022 The Authors. Advanced Energy and Sustainability Research published by Wiley-VCH GmbH. This is an open access article under the terms of the Creative Commons Attribution License, which permits use, distribution and reproduction in any medium, provided the original work is properly cited.

DOI: 10.1002/aesr.202200002

materials also had a tremendous effect in improving the FOMs of OPDs.<sup>[39,40]</sup> Fullerene-based acceptors are gradually getting replaced with non-fullerene acceptors (NFAs), a trend that has been adopted in organic photovoltaic (OPV) devices.<sup>[41,42]</sup>

In comparison to the photodetection in visible wavelength range, near-infrared (NIR) or shortwave infrared (SWIR) photodetection poses serious challenges, mainly due to the significantly high thermal generation of  $J_d$ .<sup>[43]</sup> The high  $J_d$  limits the signal-to-noise ratio, which in turn affects  $D^*$ . It is extremely difficult to determine the exact origin of noise in disordered organic systems and the net result is sometimes the erroneous estimation of noise current ( $i_n$ ) and unrealistic values of  $D^*$ . Thus, finding the origin of dark/noise current and estimating a reasonable upper limit for  $D^*$  are critical. In these directions, a number of in-depth and systematic studies are reported with physical process insights. Findings/observations from these studies will guide future material/device architecture innovations and shed light on the limits and possibilities in OPDs.

So far, the majority of the review articles in OPD are revolving around the progress in performance metrics,<sup>[44,45]</sup> innovations in material design/device engineering,<sup>[46]</sup> potential applications in wearable technologies, and so on.<sup>[30]</sup> Thus, a review that substantiates the progress in physical process understanding is highly important. Here, we present an overview of the updated advances related to trap-states, charge transfer (CT) states, and noise/detectivity limits in organic photodiodes. Insights on the fundamental limiting factors and theoretical performance limits will offer targets for future work on maximizing key performance metrics. It is to be noted that the performance metrics of OPDs are widely described in the literature, and we neglect to duplicate them here.<sup>[30,47]</sup> In this review, the organic photodetectors refer to organic photodiodes unless otherwise specified.

## 2. Role of Trap-States in OPD Performance Metrics

The understanding of traps remains a heavily debated and controversial topic in organic optoelectronics due to the amorphous nature of organic materials.<sup>[48,49]</sup> Trap states and recombination through trap-states were frequently reported in organic bulk heterojunction (BHJ) solar cells. In organic BHJ, the separated charges moving through percolating paths toward the respective electrodes may interfere distributed “defective or impurity sites” of lower energy, called trap states.<sup>[50]</sup> The moving charge may be confined to these trap states for a time interval that may depend upon the trap depth and temperature of the system.<sup>[50]</sup> These trap states were described as either mid-gap states or the shallow tail states lying below the transport gap.<sup>[51–53]</sup> Trap states were shown to have important consequences on the charge carrier dynamics of OPV devices. The influence of traps on the performance metrics of OPD is an important aspect to be considered, but relatively less explored. There are a limited number of reports investigating the trap dynamics and their effect on the electrical response of OPDs. Conclusions drawn from these modeling/experimental studies will assist in the future performance optimization strategies. The following section highlights the important studies that explore the role of trap states in  $J_d$  and the temporal response of OPDs.

$J_d$  is typically the fundamental parameter that influences the sensitivity of a photodetector. There were enormous efforts to suppress  $J_d$  to a minimum range. These efforts include the use of charge blocking layers, thick active layers to reduce the shunt pathways, contact alignment, etc.<sup>[54–58]</sup> The aforementioned approaches have resulted in low  $J_d$  at relatively low reverse biases.<sup>[54,56]</sup> Still, in most reported cases,  $J_d$  scales proportionally with increasing reverse bias voltage.<sup>[59]</sup>  $J_d$  values in low-bandgap OPD systems are still orders of magnitude higher than those in IPDs. Thus, comprehensive studies into the intrinsic and extrinsic sources of  $J_d$  are imperative for the proficient optimization of OPD performance. Fallahpour et al. developed a comprehensive model that can describe the OPD device operation under various light illumination intensities and explained the critical role of trap states under low light/dark conditions.<sup>[60]</sup> The classical poly(3-hexylthiophene-2,5-diyl) (P3HT): [6,6]-phenyl-C61-butyric acid methyl ester (PC<sub>61</sub>BM) system was selected for the study. Simulated current density–voltage ( $J$ – $V$ ) characteristics at higher light intensities were in good agreement with the experimental values. However, deviation in simulated to experimental values was prominent at lower light intensities ( $<1 \mu\text{W cm}^{-2}$ ) or dark. An additional loss mechanism is thus expected to act at lower light intensities. With supporting evidence, factors like effective bandgap of the material, carrier injection from the contacts were shown to have no obvious influence on the deviation from simulated to measurement values. The  $J$ – $V$  characteristics at lower intensities or in dark were reproduced when “trap-dynamics” was added to their model. These results point out that the trap density is a noticeable contributor in controlling current at lower light intensities.

The effective bandgap in OPD is a characteristic of the charge transfer state energy ( $E_{CT}$ ) formed at the donor (D)–acceptor (A) interface. Thus, the activation energy for the ideal dark current in OPD is determined by the  $E_{CT}$  value. Kublitski et al. revealed the interplay between trap state and CT state as a source of  $J_d$  in OPDs.<sup>[61]</sup> A series of optimized PD devices, based on different donor molecules blended with C<sub>60</sub> were fabricated.  $E_{CT}$  was tuned from 0.85 to 1.58 eV as indicated in the legend (Figure 1a). They found that  $J_d$  decreased with an increase in  $E_{CT}$  and achieved a value as low as  $10^{-7} \text{ mA cm}^{-2}$  at  $-1 \text{ V}$ . This value was still orders of magnitude higher than the ideal dark saturation current density ( $J_0$ , calculated from Equation (1) and (2)), within the radiative limit (Figure 1b).

$$J_0 \approx J_{SC} \exp\left(-\frac{qV_{OC}}{K_B T}\right), \quad \text{for } V_{OC} \gg \frac{K_B T}{q} \quad (1)$$

where  $J_{SC}$  is the short circuit current density under illumination,  $V_{OC}$  is the open-circuit voltage,  $K_B$  is the Boltzman constant, and  $T$  is the absolute temperature.

$$V_{OC} \approx \frac{E_{CT}}{q} - \frac{K_B T}{q} \ln \left[ \frac{2\pi q}{h^3 c^2} \frac{(E_{CT} - \lambda_{CT})}{J_{SC} \text{EQE}_{EL}} f_{CT} \right] \quad (2)$$

where  $\text{EQE}_{EL}$  is the external quantum efficiency of electroluminescence,  $\lambda_{CT}$  is the reorganization energy of the CT state, and  $f_{CT}$  is proportional to the oscillator strength of the CT transition and the density of CT states in the blend.<sup>[61,62]</sup> The discrepancy between measured  $J_d$  to the ideal, thermally generated dark

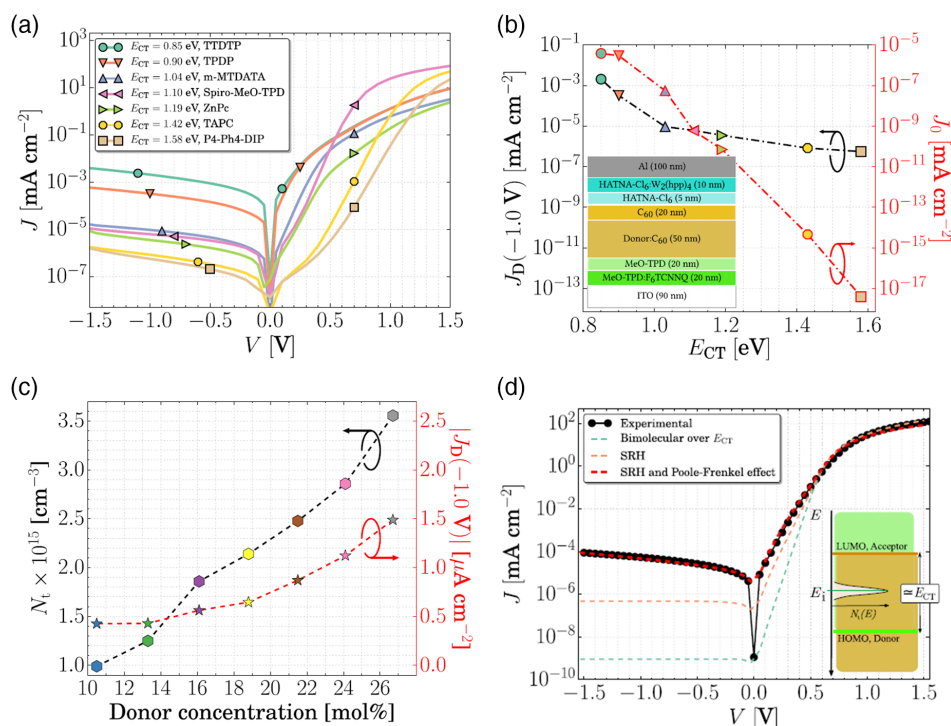


**Figure 1.** a) Dark  $J$ - $V$  characteristics of blends with different  $E_{CT}$  values. b) Difference in  $J_d$  and  $J_0$  values with varying  $E_{CT}$  range. c) Trap density and absolute  $J_d$  at different donor concentrations. d) Simulated and experimental dark  $J$ - $V$  characteristics of ZnPC:C<sub>60</sub> device. Reproduced under the terms of a Creative Commons Attribution 4.0 International License.<sup>[61]</sup> Copyright 2021, The authors, published by Springer Nature.

current density  $J_0$  is typically observed in organic PDs and in turn limits the maximum achievable  $D^*$ . The trap density and absolute  $J_d$  for different donor concentrations are shown in Figure 1c. The increase of  $J_d$  with an increase in trap density suggests that the generation of charges via trap states is contributing toward the extra-dark current. By employing drift-diffusion simulations, they found that the difference in  $J_0$  to the experimentally measured  $J_d$  can be explained if the trap distribution at the D-A blend is considered. In the absence of traps, only the charge carriers that are excited over  $E_{CT}$  can contribute to the  $J_d$  in reverse bias. This value was in a similar range to the estimated  $J_0$ . When the Shockley-Read-Hall (SRH) generation through trap state is included in the model, the  $J_d$  is increased over 3 orders. However, the value does not match with the experimental  $J_d$  in terms of magnitude and field dependence. By adding Poole-Frenkel effect along with SRH, the experimental  $J_d$  can be completely reproduced (Figure 1d). Thus, the role of traps as a major source of dark current is successfully demonstrated.

Zarrabi et al. found that the charge generating mid-gap states have important consequences in organic solar cells and photodiodes.<sup>[53]</sup> Using an ultra-sensitive external quantum efficiency (s-EQE),<sup>[53]</sup> they investigated the sub-bandgap properties of a set of BHJ D:A combinations. In addition to the CT state, they observe another charge-generating state termed as “mid-gap state” at the D:A interface, contributing to the current generation. Mid-gap states are found at the low-energy sub-gap region as a different plateau than the CT state, with roughly  $\sim$ half the energy of  $E_{CT}$ . The schematic energy-level diagram at the D-A interface

consisting of mid-gap states is depicted in Figure 2a. To understand the origin of mid-gap states, the trap-density is intentionally increased by adding a small amount of 4,4',4''-Tris(N-3-methylphenyl-N-phenyl-amino)-triphenylamine (m-MTDATA) into the active layer of poly[N-9'-heptadecanyl-2,7-carbazole-alt-5,5-(4',7'-di-2-thienyl-2',1',3'-benzothiadiazole)] (PCDTBT):PC<sub>70</sub>BM. A clear increase in the strength of the low-energy sub-gap signal is observed (compared to no m-MTDATA addition) in ultra-sensitive EQE spectra. The aforementioned observation indicates that the low-energy sub-gap feature is associated with charge trapping in mid-gap states. Using a two-diode model, good agreement between the simulated and experimental dark  $J$ - $V$  characteristics of a photodiode is demonstrated. Dark  $J$ - $V$  curves considering Shockley-Queisser (SQ) limit (also known as background-limited infrared photodetection (BLIP) limit), radiative CT state limit ( $CT_R$ ), nonradiative CT state limit ( $CT_{NR}$ ), and trap states are constructed and the respective shot-noise limited detectivity at 500 nm is calculated (Figure 2b-d). It is important to note that the estimated thermodynamic limit of  $D^*$  is several orders of magnitude lower than the one estimated without considering the mid-gap state. This work solidifies the prior findings of trap-state contribution to the dark current.

To understand the influence of trap state on the temporal response of the OPD, Popescu and co-workers studied the  $-3$  dB cutoff frequency of OPD under varying light intensities, reaching as low as nW cm<sup>-2</sup>.<sup>[63]</sup> They fabricated two types of OPD devices with the only difference being the hole extraction layers. Poly(3,4-ethylenedioxythiophene): polystyrene sulfonate

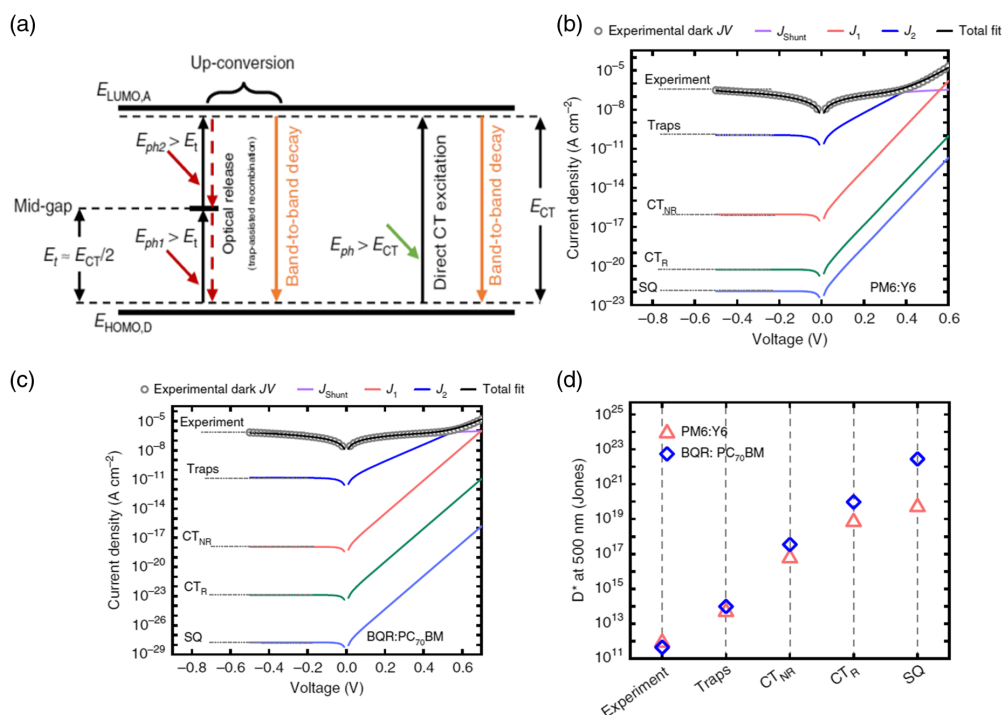


**Figure 2.** a) Schematic energy level diagram of D–A interface including the mid-gap state. The experimental dark  $J$ – $V$  and the dark  $J$ – $V$  contributions from different limiting recombination processes for: b) PM6:Y6 system and c) BQR:PC<sub>70</sub>BM system. d) Shot-noise limited specific detectivity of two different blends at 500 nm considering different limiting factors. Reproduced under the terms of a Creative Commons Attribution 4.0 International License.<sup>[53]</sup> Copyright 2020, The authors, published by Springer Nature.

(PEDOT:PSS) or P3HT were used as hole extraction layers. A nonlinear and nonconstant  $-3$  dB cutoff frequency was observed over the varying illumination intensity range and PEDOT:PSS-based device exhibits more severe decay than P3HT-based device. To reproduce these experimental results, a model based on drift-diffusion is proposed. Multiple trapping/de-trapping effects at the interface and in the bulk were carefully integrated into the model. By successfully reproducing the experimental results with the proposed model, they conclude that the nonlinearity in  $-3$  dB frequency is mainly caused by the position, concentration, and distribution of trap states at the interface between BHJ and hole extraction layer. Using appropriate interface engineering, the frequency response in the kHz regime was demonstrated at low light intensities ( $20 \text{ nW cm}^{-2}$ ).<sup>[49]</sup> Their results point out the importance of the selection of low-trap density charge extraction layers and the modification of interfaces for achieving linear and constant temporal responses, especially at low light intensities.

### 3. Manipulation of Charge-Transfer States

An intermolecular CT state is formed at the interface between electron donor material and electron acceptor material in an organic bulk/planar heterojunction. It has serious implications on organic solar cells,<sup>[64,65]</sup> light-emitting diodes,<sup>[65]</sup> and detectors.<sup>[66]</sup> CT states mediate the charge separation and charge recombination processes.<sup>[67]</sup> In OPV devices, high open-circuit

voltage ( $V_{OC}$ ) is targeted by selecting a D–A combination with high  $E_{CT}$ , which is close to the optical bandgap of the low-bandgap absorber.<sup>[68]</sup> When it comes to OPDs, intermolecular CT state absorption may be exploited to realize extended absorption capabilities much longer than the corresponding neat D or A materials. Since the CT state has lower transition energy, it can potentially absorb light with photon energy below the bandgap of the constituent parental materials.<sup>[69]</sup> However, being an intermolecular state, the absorption strength of the CT state is rather poor, at least two orders lower than the singlet absorption.<sup>[70]</sup> To make use of the CT state absorption, thick active layers of tens of  $\mu\text{m}$  thickness should be employed. This approach might not result in reasonable optoelectronic performance, as extremely high voltage is required to extract the charges efficiently. Thus, innovative ways of light trapping are demanded to amplify the CT state absorption. This section overviews the studies exploiting CT state absorption to realize efficient NIR-sensitive OPDs.

Siegmund et al. found an exciting way of manipulating the CT state absorption to design narrowband photodetectors.<sup>[71]</sup> Direct intermolecular CT absorption is generally neglected due to its weak nature. However, utilizing CT absorption has the advantage that the detection wavelength can be easily extended far beyond the pristine absorber materials. A microcavity architecture is introduced to amplify the typically negligible sub-bandgap EQE up to 40 times (peak values  $>20\%$ ) with a spectral width as low as 36 nm, enabling narrowband photodetection. Here, the microcavity formation is guided by fully reflective and



partially transmissive silver mirrors and the resonance wavelength can be easily tuned by varying the cavity thickness (Figure 3a). The simplified energy level diagram of the cavity-enhanced device is given in Figure 3b. By employing different donors to pair with  $C_{60}$ , the resonance wavelength can be extended over a broad range (up to 1550 nm) (Figure 3c). The proof-of-concept device utilizes the weak absorbing nature of the CT state to realize narrowband absorption, while using the cavity structure to enhance the EQE. Kaiser et al. further extended the resonance wavelength range using the rational molecular design of the D material.<sup>[72]</sup> When the functionalized D material is blended with the  $C_{60}$  acceptor, the cavity-enhanced NIR OPD exhibits an extended operational window from 810 to 1665 nm.

It is to be noted that, in principle, optical cavities can result in unity EQE values, but are practically diminished by parasitic absorption. Tang and coworkers found effective solutions to this issue and boosted the EQE values in the CT spectroscopic range.<sup>[73]</sup> As a major step, a blend with a high degree of intermixing and appropriate CT absorption strength (PBTBT:PCBM) was employed to fabricate a narrowband microcavity architecture OPD. In addition, increasing the order of resonance ( $>1$ ) by using a thicker active layer was also demonstrated as an effective strategy to improve the EQE. To further reduce parasitic absorption, an alternative electrode with high reflectivity and lower parasitic absorption is highly desirable. Thus, high

conductivity PEDOT:PSS PH100-coated distributed Bragg reflectors (DBRs) were used as the back reflecting electrode. The spectral selectivity was further improved to an FWHM value as low as 14 nm. Combining the merits of intercalation between absorbing layers, higher order resonance, and DBR based back reflecting electrode, the proof-of-concept OPD device exhibits attractive FOMs like  $D^*$  over  $10^{13}$  Jones, LDR  $> 130$  dB, and fast response time of 230 ns.

Since the microcavity enhanced narrowband OPD devices utilizing CT absorption were shown to have excellent sensitivity, Ullbrich et al. focused on maximizing its temporal response characteristics.<sup>[74]</sup> In the case of ZnPc/ $C_{60}$  blend-based microcavity OPD, the major limiting factor for high-frequency response is shown as the extraction of holes. Thus, optimizing the travel distance for both holes and electrons is shown to be the key to maximize the detector response, and the  $-3$  dB frequency response was enhanced up to 68 MHz using a planar mixed heterojunction (PMHJ) design. The  $-3$  dB frequency of tens of MHz and fall time of a few nanoseconds remain as one among the best-reported values in OPD.<sup>[45]</sup>

Inspired by the microcavity architecture, Gibert-Roca et al. employed a photonic architecture to enhance the CT absorption and demonstrated a NIR OPD.<sup>[75]</sup> In this work, the active layer was deposited by blade coating, and the dry active layer was nanostructured via the nanoimprinting lithography technique. The as-produced pattern acted as a diffraction grating, coupling the incident light into the active layer propagating modes. The CT absorption was thus amplified by the light trapping below the bandgap of the BHJ blend. Overall, the OPD based on photonic device structure exhibits appreciable performance metrics. In comparison with the microcavity architecture, this device structure is insensitive to the active layer thickness variation and offers appealing fabrication tolerance.

Kim et al. achieved narrowband NIR absorption via intermolecular CT-mediated coupling without optically fine-tuning the device architecture.<sup>[76]</sup> In this work, a squaraine (SQ-H) dye was used as a donor material in combination with PC<sub>61</sub>BM to fabricate the proof-of-concept OPD. Compared to the as-cast SQ-H film with a broad absorption spectrum, the SQ-H annealed film possesses bathochromically shifted longer wavelength narrowband absorption. These prominent changes in the absorption spectrum are attributed to the strong intermolecular interaction occurring upon aggregation. The resulting narrowband OPD with well-organized nanocrystalline bulk heterojunction exhibits  $\approx 12\%$  EQE at 1050 nm, an appreciable value considering its origin from intermolecular CT-mediated coupling.

Hybrid heterojunction consisting of inorganic and organic materials was previously explored for applications in optoelectronic devices.<sup>[77]</sup> The performance metrics of these devices were barely encouraging, and the lower performance was attributed to poor charge generation and the presence of trap states.<sup>[78–81]</sup> However, Eisner and coworkers recently used inorganic/organic hybrid junctions to realize a high-performance NIR photodetector.<sup>[82]</sup> Unlike the typically explored metal oxide/organic heterojunctions, a range of less studied “copper thiocyanates (e.g., CuSCN, a p-type inorganic semiconductor)/organic” hybrid heterojunctions are investigated to understand the charge generation mechanism (Figure 4a). The normalized EL emission spectrum and normalised EQE spectrum of PEDOT:PSS/ 3,9-bis

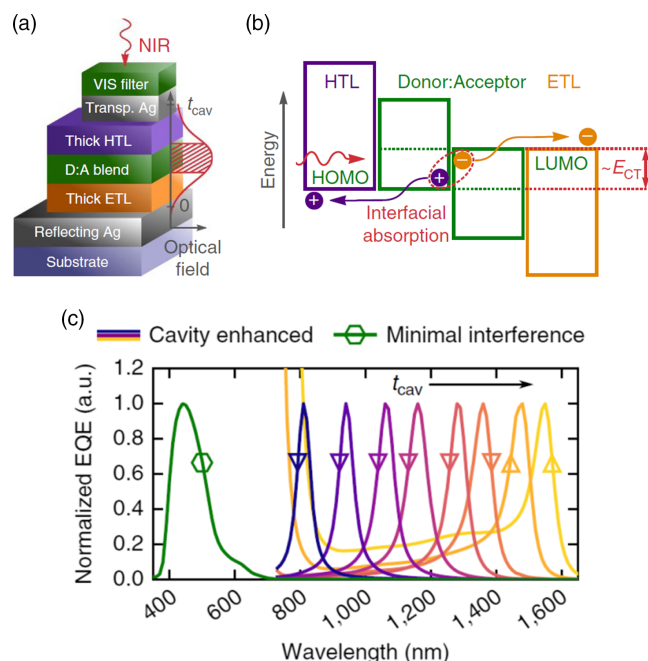


**Figure 3.** a) Simplified device architecture of cavity-enhanced photodiode. b) Simplified energy-level diagram with the demonstration of photon absorption, charge generation, and charge transport processes. c) Normalized EQE spectra of a reference photodiode (minimal interference) and a photodiode with microcavity structure (enhanced optical cavity). Resonance wavelength was tuned by varying the transport layer and/or active layer thicknesses. Reproduced under the terms of a Creative Commons Attribution 4.0 International License.<sup>[71]</sup> Copyright 2017, The authors, published by Springer Nature.

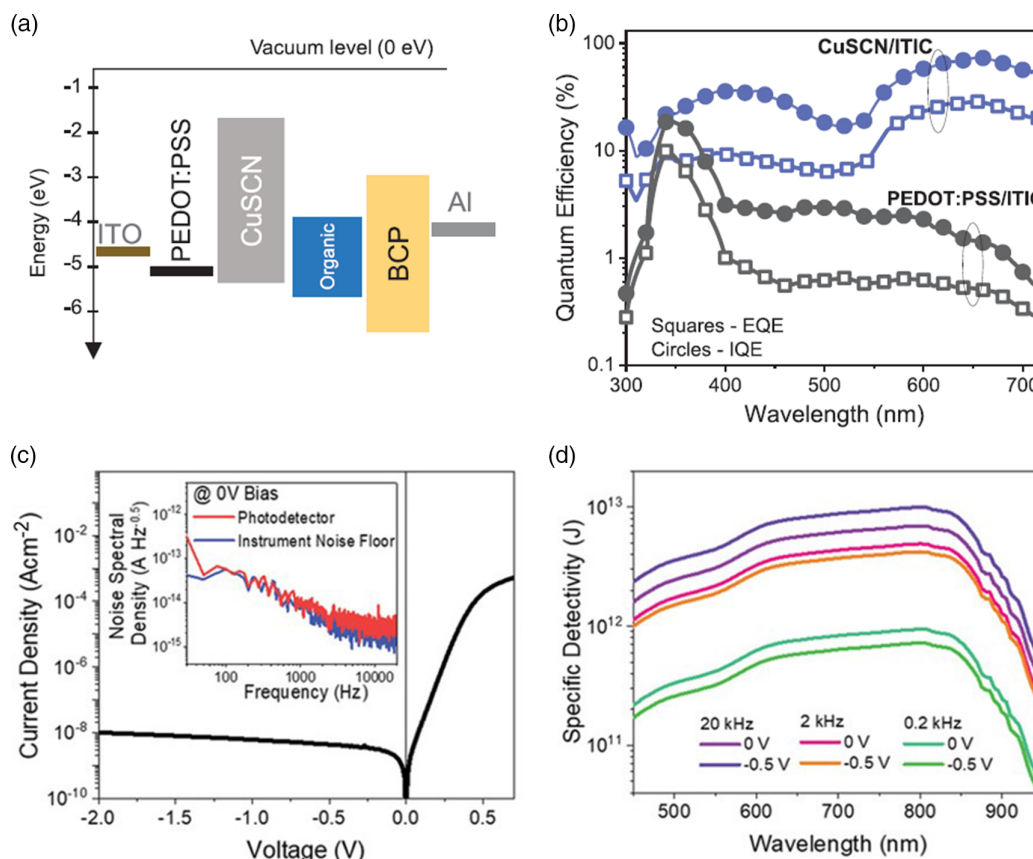


**Figure 4.** a) Energy-level diagram of the materials used in the study. Type-2 (staggered gap) heterojunction is formed at the CuSCN/organic interface. b) Quantum efficiency of CuSCN/ITIC and PEDOT:PSS/ITIC devices. (c) Dark  $J$ - $V$  characteristics and noise-spectral density of CuSCN/organic photodiode and d)  $D^*$  of the CuSCN/organic photodiode. Reproduced under the terms of a Creative Commons Attribution 4.0 International License.<sup>[82]</sup> Copyright 2021, The authors, published by Wiley-VCH GmbH.

(2-methylene-(3-(1,1-dicyanomethylene)-indanone))-5,5,11,11-tetrakis(4-hexylphenyl)-dithieno[2,3-d':2',3'-d'']-s-indaceno[1,2-b:5,6-b']dithiophene (ITIC) and CuSCN/ITIC heterojunctions are studied in detail. CuSCN/ITIC sub-bandgap absorption shows a more extended, shallow absorption tail that extends beyond the absorption tail of ITIC. The high-intensity emission from the low-energy state of CuSCN/ITIC heterojunction device implies that these states are emissive CT states, since traps typically act as nonradiative pathways for recombination. The internal quantum efficiency (IQE) and EQE of CuSCN/ITIC and PEDOT:PSS/ITIC are shown in Figure 4b. The IQE of CuSCN/ITIC device is  $\approx 70\%$  in the region where ITIC has strong absorption, suggesting efficient charge separation efficiency at the inorganic/organic interface. However, the IQE of PEDOT:PSS/ITIC device was negligible throughout the wavelength range due to the inefficient interface for charge separation. These observations suggest that the charge generation in CuSCN/ITIC proceeds through an emissive CT state, the first report of its kind in inorganic/organic HJ, and the charge generation is efficient due to the facile CT exciton dissociation at the interface. These heterojunctions exhibit ultralow nonradiative voltage losses and high IQEs in solar cells. It has been reported that the nonradiative recombination dominates the dark

saturation current in photodetectors and in turn limits  $D^*$ .<sup>[61]</sup> A highly sensitive NIR OPD is realized using these advantageous characteristics of CuSCN/organic HJ, exhibiting low  $J_d$ , excellent  $D^*$  just under  $10^{13}$  Jones, LDR over 130 dB, and reasonable temporal response (Figure 4c,d).

#### 4. Noise/Detectivity Limits

Photodetector sensitivity is the most widely used metric by which the performance of a particular photodetector is quantified and compared with other photodetectors.<sup>[83]</sup> The basic metric which relates to the sensitivity is noise current ( $i_n$ , in units of  $A\ Hz^{-1/2}$ ).<sup>[44]</sup> Any current generated without light or signal defines the noise level, which determines the minimum detectable signal of photodetectors.<sup>[44]</sup> These random fluctuations contain shot noise, thermal noise,  $1/f$  noise, and generation-recombination (g-r) noise components.<sup>[44]</sup> The noise current can be expressed as follows

$$i_n = \sqrt{i_{\text{shot}}^2 + i_{\text{thermal}}^2 + i_{1/f}^2 + i_{g-r}^2} \quad (3)$$

For the accurate estimation of specific detectivity ( $D^*$ ), the  $i_n$  should be carefully measured experimentally.

$D^*$  defines the ability to detect faint optical signals and is given by Equation (4)

$$D^* = \frac{\sqrt{A}}{NEP} = \frac{R\sqrt{A}}{i_n} \quad (4)$$

where  $A$  is the area in  $\text{cm}^2$ ,  $NEP$  is noise equivalent power in  $\text{W Hz}^{-1/2}$ ,  $R$  is the responsivity in  $\text{A W}^{-1}$ , and  $i_n$  is the noise current.<sup>[30]</sup>  $R$  is given by the Equation (5) as

$$R = \frac{EQE}{100\%} \times \frac{\lambda}{1240(\text{nm W A}^{-1})} \quad (5)$$

where  $\lambda$  is the wavelength in nm.<sup>[37]</sup> Equation (4) and (5) convey that the key to high  $D^*$  is the low  $i_n$  and high EQE. However, high noise and low photovoltaic EQE negatively influence  $D^*$  in the longer wavelength region and limit the low light performance of OPD.<sup>[31,84,85]</sup>  $D^*$  of current OPD devices is orders of magnitude lower than the BLIP limit, which assumes an EQE of 100% and background radiation as the only noise.

To extend the detection capabilities to the NIR and SWIR regions, the usage of narrow-bandgap photoactive materials is a prerequisite.<sup>[86]</sup> But these materials usually suffer from high dark and noise currents and the values typically increase with decreasing optical bandgap, limiting overall  $D^*$ .<sup>[43,87,88]</sup> To evolve as a potential alternative to IPD in light detection,  $D^*$  limiting factors should be identified and a reasonable thermodynamic upper limit for  $D^*$  should be defined. In this section, we overview the studies that define noise/ $D^*$  limits and the spectral range up to which a reliable photodetection is viable using OPD.

Wu and coworkers reported systematic experimental and modeling studies on noise current in a series of 10 organic

BHJ photodiodes consisting of fullerene and non-fullerene acceptors.<sup>[89]</sup> Significant noise suppression and higher  $D^*$  were found in NFA systems in comparison with fullerene systems, attributed to the low-bandtail disorder in NFAs. The dark  $J$ - $V$  characteristics of the fullerene system (polymer:PC<sub>70</sub>BM) and non-fullerene systems (polymer:ITIC-M and polymer:ITIC-F) are shown **Figure 5a**. The fullerene system has a large  $J_d$  in comparison with the NFA systems. The same trend is been continued in case of the  $i_n$  and the corresponding  $D^*$  values (Figure 5b,c). The bandtail disorder spread for these BHJ systems was estimated by fitting the density of states (DOS) data to Equation (6).

$$DOS(E_w) = N_T \exp\left(\frac{-E_w}{\Delta E}\right) + \frac{N_G}{\sigma\sqrt{2\pi}} \exp\left(-\frac{(E_w - E_{G0})^2}{2\sigma^2}\right) \quad (6)$$

The first term of the equation denotes the exponential bandtail where  $N_T$  is the DOS near the mobility edge and  $\Delta E$  is the bandtail disorder spread.  $N_G$  denotes the DOS for deep traps,  $\sigma$  is the Gaussian disorder spread and  $E_{G0}$  is the mean energy of deep traps in the second Gaussian term.<sup>[89]</sup>  $\Delta E$  for the Fullerene and NFA systems are estimated as follows: polymer:PC<sub>70</sub>BM (50 meV), polymer:ITIC-M (35 meV) and polymer:ITIC-F (29 meV).  $\Delta E$  values of fullerene system is higher than the NFA systems and explains the  $i_n$  difference in Figure 5b. The low-bandtail disorder in NFAs translates into a lower concentration of sub-bandgap states that can be occupied; resulting in the suppression of thermal generation of carriers, and in turn the reduction in thermal noise current. Considering the prominent role of disorder, a model is developed to explain the thermal noise dependence on the degree of disorder and the effective bandgap. The measured thermal noise-current on a variety of BHJ blends was successfully modeled when the energetic

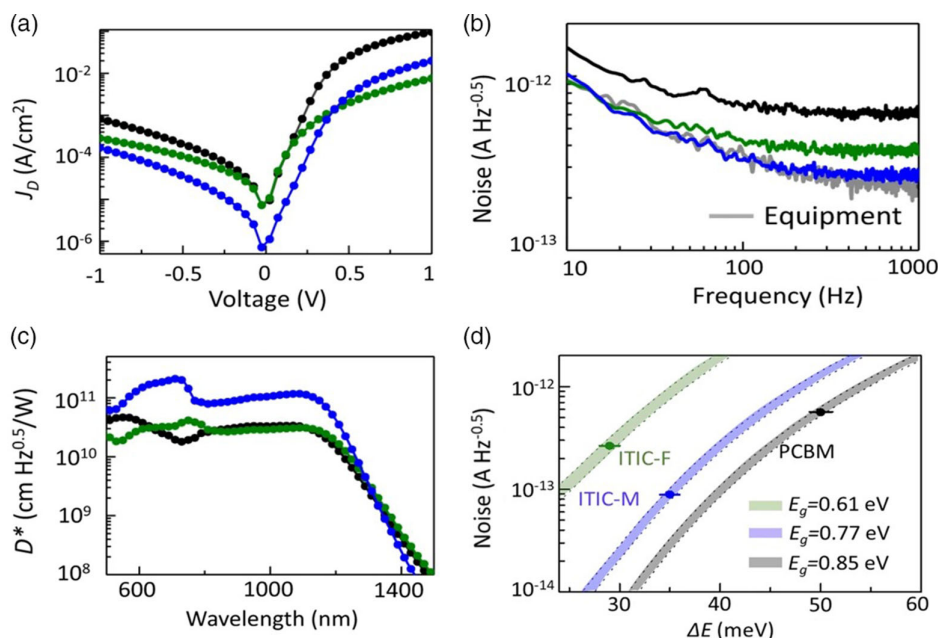


**Figure 5.** a)  $J$ - $V$  characteristics, b) noise current, and c)  $D^*$  of Polymer: ITIC-M (blue), polymer: PCBM (black), and polymer: ITIC-F (green) blends. d) Thermal noise predicted from the proposed model. The dots indicate the measured thermal noise for different photodiodes. The horizontal bars represent  $\pm 1$  meV uncertainties in the measured  $\Delta E$  values. Reproduced under the terms of a Creative Commons Attribution 4.0 International License.<sup>[89]</sup> Copyright 2020, The authors, published by Springer Nature.



disorder and effective bandgap  $E_{CT}$  were considered (Figure 5d). The model predicts that the maximum  $D^*$  is at least one order of magnitude lower than the BLIP limit, and a realistic disorder spread of 35 meV would reduce the  $D^*$  by at least two orders of magnitude. Minimizing bandtail disorder is shown to be the key in reducing the noise that is inherent to organic materials, and this approach can complement the existing noise reduction strategies.

In a different approach, Gielen et al. found nonradiative dark saturation current as the major factor limiting the  $D^*$ .<sup>[90]</sup> By investigating four low-bandgap donor polymer-based BHJ OPD devices,  $V_{OC}$  is shown to be related to  $J_d$ ,  $i_n$ , NEP, and in turn to the maximum achievable  $D^*$ .  $V_{OC}$  versus  $I_{ph}/I_D$  and  $E_{CT}$  versus  $I_D$  semilogarithmic plots for the four studied material blends and a large set of reported BHJs were analyzed, and observed a linear relationship at  $V_{OC}$  below 0.25 V and  $E_{CT}$  below 0.9 V (Figure 6a,b). These observations indicate that in low- $E_{CT}$  BHJ systems, the lowest achievable dark current at reverse bias is set by the  $V_{OC}$ . As the

lowest achievable dark current is limited by  $V_{OC}$ , factors limiting  $V_{OC}$  will have prime importance in deciding the  $D^*$  limits. Among the  $V_{OC}$  limiting factors,<sup>[91–93]</sup> nonradiative losses are proven to be the most prominent factor in deciding the upper limits of  $D^*$ .  $\Delta V_{OC,nr}$  as a function of  $E_{CT}$  is given in Figure 6c. The intrinsic upper limits for  $D^*$  at 1500 and 2000 nm are, respectively, calculated as  $10^{12}$  and  $10^{10}$  Jones (Figure 6d). In comparison to the BLIP for perfectly radiative materials,  $D^*$  values at these wavelengths are at least 3–4 orders lower.

Using state-of-the-art SWIR bulk heterojunction photodiodes, Wu et al. proposed an improved model to explain the electric field-dependence of the photocurrent for SWIR photodiodes.<sup>[94]</sup> The existing Hecht model can often reproduce the  $J$ - $V$  characteristics of the typical organic BHJ made from large bandgap systems but cannot account for the low-bandgap systems. The Hecht model generally attributes the electric field dependence to the recombination losses during charge collection and assumes a constant exciton dissociation efficiency over

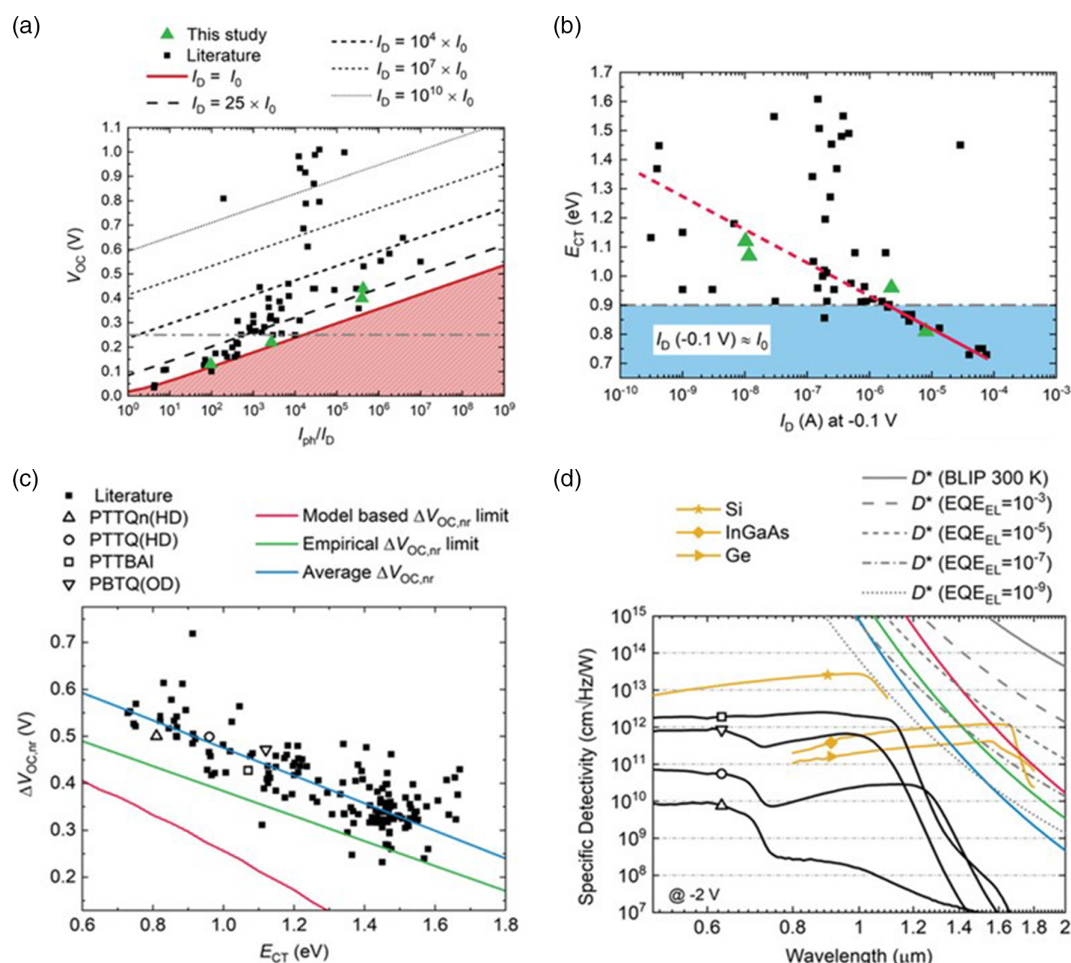


**Figure 6.** a) The calculated ratio of  $I_{ph}$  to  $I_D$  is plotted against the experimental  $V_{OC}$  in a semilogarithmic plot. b) The  $E_{CT}$  is plotted against the  $I_D$  ( $-0.1$  V) in a semilogarithmic scale. The green symbol represents the devices studied in the work and the black symbol belongs to BHJ systems reported in the literature. c)  $\Delta V_{OC,nr}$  as a function of  $E_{CT}$  in which the hollow symbols represent the BHJ systems analyzed in this work and solid black symbols belong to the literature BHJ systems. d)  $D^*$  as a function of wavelength. The red line represents the model-based  $\Delta V_{OC,nr}$  limit,<sup>[95]</sup> the green line belongs to a previously reported  $\Delta V_{OC,nr}$  empirical limit,<sup>[96]</sup> and the blue line represents the average value of  $\Delta V_{OC,nr}$  observed in this study. Reproduced under the terms of a Creative Commons Attribution 4.0 International License.<sup>[90]</sup> Copyright 2020, The authors, published by Wiley-VCH GmbH.



all-electric fields. Due to its lower built-in electric field, low-lying CT state energy, and thermal decay of CT excitons, the exciton dissociation probability is lower in SWIR devices. Thus, the proposed physical model accounts for the electric field dependence of both exciton dissociation and charge collection processes. With the help of transient photoconductivity measurements, the major loss factor in photodiodes with low  $E_{CT}$  states is identified as poor exciton dissociation efficiency. Thermal generation is significant in SWIR systems and overtakes shot noise as the dominant noise source. To account for the noise from all sources, the  $D^*$  is estimated from the experimentally measured noise characteristics. Finally, peak  $D^*$  of  $5 \times 10^{10}$  Jones is realized in SWIR photodiodes with a spectral range up to 1550 nm.

## 5. Conclusions and Outlook

Organic photodetectors are promising due to their flexibility, stretchability, biocompatibility, low-cost manufacturing, and attractive performance metrics. Along with material and device concept innovations, investigations into the performance limiting factors must be prioritized for further advances in the field. Though the visible range OPD exhibits comparable performance (except temporal response) to inorganic counterparts, the NIR/SWIR-sensitive photodetection is not mature and faces multiple challenges.

Sub-bandgap states like trap state and CT state have important roles in the performance of OPD devices, but attracted less attention. The position, concentration, and distribution of trap states have noticeable consequences on the dark current and dynamic response of OPDs. More in-depth studies related to the influence of trap states on different material systems, in particular, long-wavelength OPD systems are necessary for further improvement in device performance and stability. Beyond dark current and dynamic response, trap state influence on other OPD performance metrics should be investigated. While this concise review focuses only on photodiode-type organic photodetectors, the deciding role of trap states on the performance metrics of novel PM-type photodetectors has to be further explored with significant importance.

So far, the majority of the reported OPDs adopted material systems and device architectures similar to OPV. Exploring novel device structures and their underlying design principles is thus crucial for extending the light detection capabilities to long and spectrally selective wavelength ranges. For example, CT state is heavily exploited in organic photovoltaics, but less explored in photodetectors. The effective utilization of this sub-bandgap state is carried out by the amplification of CT absorption to realize efficient narrowband OPDs.

Based on different models, detectivity limits and the wavelength up to which a reliable photodetection is feasible are proposed. The major limiting factors for specific detectivity are shown to be nonradiative dark saturation current and band-tail disorder. More efforts should be devoted to improve the performance metrics of various material systems to the defined practical performance limits. In short, understanding of trap density, CT state, and noise/detectivity limits will positively influence the future optimization and design of efficient OPDs.

## Acknowledgements

This work was supported by the following grants: Research Grants Council of Hong Kong (GRF grant 15221320, CRF C5037-18G), National Science Foundation of China (NSFC 51961165102), Shenzhen Science and Technology Innovation Commission (Project No. JCYJ20200109105003940), and the Hong Kong Polytechnic University (The Sir Sze-yuen Chung Endowed Professorship Fund (8-8480) and Postdoc Matching Fund scheme (1-W15V)).

## Conflict of Interest

The authors declare no conflict of interest.

## Keywords

charge transfer states, noise current, organic photodiodes, specific detectivity, trap states

Received: January 4, 2022

Revised: January 31, 2022

Published online: February 26, 2022

- [1] E. O. Polat, G. Mercier, I. Nikitskiy, E. Puma, T. Galan, S. Gupta, M. Montagut, J. J. Piqueras, M. Bouwens, T. Durduran, *Sci. Adv.* **2019**, *5*, 7846.
- [2] F. Zhuge, Z. Zheng, P. Luo, L. Lv, Y. Huang, H. Li, T. Zhai, *Adv. Mater. Technol.* **2017**, *2*, 1700005.
- [3] N. Gusarova, N. Koshchavtsev, S. Popov, *J. Commun. Technol. Electron.* **2016**, *61*, 1211.
- [4] N. Li, Z. Lan, Y. S. Lau, J. Xie, D. Zhao, F. Zhu, *Adv. Sci.* **2020**, *7*, 2000444.
- [5] M. Nazhamaiti, H. Xu, Z. Liu, Y. Chen, Q. Wei, X. Wu, F. Qiao, *IEEE Trans. Circuits Syst. I. I. Express Briefs* **2021**, *68*, 3078.
- [6] R. D. Jansen-van Vuuren, A. Armin, A. K. Pandey, P. L. Burn, P. Meredith, *Adv. Mater.* **2016**, *28*, 4766.
- [7] J.-H. You, S. Oh, J.-E. Park, H. Song, Y.-K. Kim, *Measurement* **2021**, *183*, 109817.
- [8] M. Casalino, G. Coppola, M. Iodice, I. Rendina, L. Sirleto, *Sensors* **2010**, *10*, 10571.
- [9] M. Casalino, G. Coppola, M. Iodice, I. Rendina, L. Sirleto, *Int. J. Photoenergy* **2012**, *2012*, 1.
- [10] G. Konstantatos, *Nat. Commun.* **2018**, *9*, 1.
- [11] L. Shen, Y. Zhang, Y. Bai, X. Zheng, Q. Wang, J. Huang, *Nanoscale* **2016**, *8*, 12990.
- [12] R. J. Bruening, *Appl. Opt.* **1987**, *26*, 1051.
- [13] R. Wolffenbuttel, *IEEE Electron Device Lett.* **1987**, *8*, 13.
- [14] M. Ahmadi, T. Wu, B. Hu, *Adv. Mater.* **2017**, *29*, 1605242.
- [15] C. Wang, X. Zhang, W. Hu, *Chem. Soc. Rev.* **2020**, *49*, 653.
- [16] C. Li, H. Wang, F. Wang, T. Li, M. Xu, H. Wang, Z. Wang, X. Zhan, W. Hu, L. Shen, *Light Sci. Appl.* **2020**, *9*, 1.
- [17] Y. Liu, M. Pharr, G. A. Salvatore, *ACS Nano* **2017**, *11*, 9614.
- [18] T. Q. Trung, N. E. Lee, *Adv. Mater.* **2016**, *28*, 4338.
- [19] T. Yokota, P. Zalar, M. Kaltenbrunner, H. Jinno, N. Matsuhisa, H. Kitanosako, Y. Tachibana, W. Yukita, M. Koizumi, T. Someya, *Sci. Adv.* **2016**, *2*, e1501856.
- [20] J. Liu, Y. Wang, H. Wen, Q. Bao, L. Shen, L. Ding, *Solar RRL* **2020**, *4*, 2000139.
- [21] D. Yang, D. Ma, *Adv. Opt. Mater.* **2019**, *7*, 1800522.
- [22] A. Falco, L. Cinà, G. Scarpa, P. Lugli, A. Abdellah, *ACS Appl. Mater. Interfaces* **2014**, *6*, 10593.

- [23] I. Ashraf, A. A. El-Zahhar, A. M. Idris, F. B. Ahmed, *Optik* **2021**, 242, 167247.
- [24] Z. Zhao, M. Liu, K. Yang, C. Xu, Y. Guan, X. Ma, J. Wang, F. Zhang, *Adv. Funct. Mater.* **2021**, 31, 2106009.
- [25] M. Liu, J. Wang, K. Yang, Z. Zhao, Z. Zhou, Y. Ma, L. Shen, X. Ma, F. Zhang, *J. Mater. Chem. C* **2021**, 9, 6357.
- [26] K. Yang, Z. Zhao, M. Liu, Z. Zhou, K. Wang, X. Ma, J. Wang, Z. He, F. Zhang, *Chem. Eng. J.* **2022**, 427, 131802.
- [27] W. Wang, F. Zhang, M. Du, L. Li, M. Zhang, K. Wang, Y. Wang, B. Hu, Y. Fang, J. Huang, *Nano Lett.* **2017**, 17, 1995.
- [28] W. Wang, M. Du, M. Zhang, J. Miao, Y. Fang, F. Zhang, *Adv. Opt. Mater.* **2018**, 6, 1800249.
- [29] M. Liu, J. Wang, Z. Zhao, K. Yang, P. Durand, F. Ceugniet, G. Ulrich, L. Niu, Y. Ma, N. Leclerc, *J. Phys. Chem. Lett.* **2021**, 12, 2937.
- [30] P. C. Chow, T. Someya, *Adv. Mater.* **2020**, 32, 1902045.
- [31] K. J. Baeg, M. Binda, D. Natali, M. Caironi, Y. Y. Noh, *Adv. Mater.* **2013**, 25, 4267.
- [32] C. Fuentes-Hernandez, W.-F. Chou, T. M. Khan, L. Diniz, J. Lukens, F. A. Larrain, V. A. Rodriguez-Toro, B. Kippelen, *Science* **2020**, 370, 698.
- [33] B. Xie, R. Xie, K. Zhang, Q. Yin, Z. Hu, G. Yu, F. Huang, Y. Cao, *Nat. Commun.* **2020**, 11, 1.
- [34] A. Armin, R. D. Jansen-van Vuuren, N. Kopidakis, P. L. Burn, P. Meredith, *Nat. Commun.* **2015**, 6, 1.
- [35] Z. Lan, Y. Lei, W. K. E. Chan, S. Chen, D. Luo, F. Zhu, *Sci. Adv.* **2020**, 6, 8065.
- [36] Z. Lan, Y. S. Lau, Y. Wang, Z. Xiao, L. Ding, D. Luo, F. Zhu, *Adv. Opt. Mater.* **2020**, 8, 2001388.
- [37] J. Huang, J. Lee, J. Vollbrecht, V. V. Brus, A. L. Dixon, D. X. Cao, Z. Zhu, Z. Du, H. Wang, K. Cho, *Adv. Mater.* **2020**, 32, 1906027.
- [38] Z. Zhong, F. Peng, Z. Huang, L. Ying, G. Yu, F. Huang, Y. Cao, *ACS Appl. Mater. Interfaces* **2020**, 12, 45092.
- [39] W. Li, Y. Xu, X. Meng, Z. Xiao, R. Li, L. Jiang, L. Cui, M. Zheng, C. Liu, L. Ding, *Adv. Funct. Mater.* **2019**, 29, 1808948.
- [40] J. Liu, M. Gao, J. Kim, Z. Zhou, D. S. Chung, H. Yin, L. Ye, *Mater. Today* **2021**, 51, 475.
- [41] C. Yan, S. Barlow, Z. Wang, H. Yan, A. K. Y. Jen, S. R. Marder, X. Zhan, *Nat. Rev. Mater.* **2018**, 3, 1.
- [42] J. Lee, S.-J. Ko, H. Lee, J. Huang, Z. Zhu, M. Seifrid, J. Vollbrecht, V. V. Brus, A. Karki, H. Wang, *ACS Energy Lett.* **2019**, 4, 1401.
- [43] Q. Li, Y. Guo, Y. Liu, *Chem. Mater.* **2019**, 31, 6359.
- [44] Z. Zhao, C. Xu, L. Niu, X. Zhang, F. Zhang, *Laser Photonics Rev.* **2020**, 14, 2000262.
- [45] H. Ren, J. D. Chen, Y. Q. Li, J. X. Tang, *Adv. Sci.* **2021**, 8, 2002418.
- [46] J. Liu, M. Gao, J. Kim, Z. Zhou, D. S. Chung, H. Yin, L. Ye, *Mater. Today* **2021**, 51, 475.
- [47] F. P. G. de Arquer, A. Armin, P. Meredith, E. H. Sargent, *Nat. Rev. Mater.* **2017**, 2, 1.
- [48] C. G. Shuttle, N. D. Treat, J. D. Douglas, J. M. Fréchet, M. L. Chabiny, *Adv. Energy Mater.* **2012**, 2, 111.
- [49] F. Arca, S. F. Tedde, M. Sramek, J. Rau, P. Lugli, O. Hayden, *Sci. Rep.* **2013**, 3, 1.
- [50] C. Carati, L. Bonoldi, R. Po, *Phys. Rev. B* **2011**, 84, 245205.
- [51] T. Kirchartz, B. E. Pieters, J. Kirkpatrick, U. Rau, J. Nelson, *Phys. Rev. B* **2011**, 83, 115209.
- [52] J. Wu, J. Luke, H. K. H. Lee, P. S. Tuladhar, H. Cha, S.-Y. Jang, W. C. Tsoi, M. Heeney, H. Kang, K. Lee, *Nat. Commun.* **2019**, 10, 1.
- [53] N. Zarrabi, O. J. Sandberg, S. Zeiske, W. Li, D. B. Riley, P. Meredith, A. Armin, *Nat. Commun.* **2020**, 11, 1.
- [54] A. Armin, M. Hamsch, I. K. Kim, P. L. Burn, P. Meredith, E. B. Namdas, *Laser Photonics Rev.* **2014**, 8, 924.
- [55] Z. Zhong, L. Bu, P. Zhu, T. Xiao, B. Fan, L. Ying, G. Lu, G. Yu, F. Huang, Y. Cao, *ACS Appl. Mater. Interfaces* **2019**, 11, 8350.
- [56] G. Liu, T. Li, X. Zhan, H. Wu, Y. Cao, *ACS Appl. Mater. Interfaces* **2020**, 12, 17769.
- [57] Z. Huang, Z. Zhong, F. Peng, L. Ying, G. Yu, F. Huang, Y. Cao, *ACS Appl. Mater. Interfaces* **2020**, 13, 1027.
- [58] S. Xiong, L. Li, F. Qin, L. Mao, B. Luo, Y. Jiang, Z. Li, J. Huang, Y. Zhou, *ACS Appl. Mater. Interfaces* **2017**, 9, 9176.
- [59] Y. Wei, H. Chen, T. Liu, S. Wang, Y. Jiang, Y. Song, J. Zhang, X. Zhang, G. Lu, F. Huang, *Adv. Funct. Mater.* **2021**, 31, 2106326.
- [60] A. Fallahpour, S. Kienitz, P. Lugli, *IEEE Trans. Electron Devices* **2017**, 64, 2649.
- [61] J. Kublitski, A. Hofacker, B. K. Boroujeni, J. Benduhn, V. C. Nikolis, C. Kaiser, D. Spoltore, H. Kleemann, A. Fischer, F. Ellinger, *Nat. Commun.* **2021**, 12, 1.
- [62] K. Vandewal, K. Tvingstedt, A. Gadisa, O. Inganäs, J. V. Manca, *Phys. Rev. B* **2010**, 81, 125204.
- [63] B. V. Popescu, D. H. Popescu, P. Lugli, S. Locci, F. Arca, S. F. Tedde, M. Sramek, O. Hayden, *IEEE Trans. Electron Devices* **2013**, 60, 1975.
- [64] T. W. Ng, M. F. Lo, M. K. Fung, W. J. Zhang, C. S. Lee, *Adv. Mater.* **2014**, 26, 5569.
- [65] H. T. Chandran, T. Liu, D. Shen, Z. Guan, M. Li, J. Antonio Zapien, S.-W. Tsang, M.-F. Lo, C.-S. Lee, *Solar RRL* **2020**, 4, 2000245.
- [66] S. Ullbrich, B. Siegmund, A. Mischok, A. Hofacker, J. Benduhn, D. Spoltore, K. Vandewal, *J. Phys. Chem. Lett.* **2017**, 8, 5621.
- [67] D. Shen, W.-C. Chen, M.-F. Lo, C.-S. Lee, *Mater. Today Energy* **2021**, 20, 100644.
- [68] F. D. Eisner, M. Azzouzi, Z. Fei, X. Hou, T. D. Anthopoulos, T. J. S. Dennis, M. Heeney, J. Nelson, *J. Am. Chem. Soc.* **2019**, 141, 6362.
- [69] V. Coropceanu, X.-K. Chen, T. Wang, Z. Zheng, J.-L. Brédas, *Nat. Rev. Mater.* **2019**, 4, 689.
- [70] X.-K. Chen, V. Coropceanu, J.-L. Brédas, *Nat. Commun.* **2018**, 9, 1.
- [71] B. Siegmund, A. Mischok, J. Benduhn, O. Zeika, S. Ullbrich, F. Nehm, M. Böhm, D. Spoltore, H. Fröb, C. Körner, *Nat. Commun.* **2017**, 8, 1.
- [72] C. Kaiser, K. S. Schellhammer, J. Benduhn, B. Siegmund, M. Tropanio, J. Kublitski, D. Spoltore, M. Panhans, O. Zeika, F. Ortmann, *Chem. Mater.* **2019**, 31, 9325.
- [73] Z. Tang, Z. Ma, A. Sánchez-Díaz, S. Ullbrich, Y. Liu, B. Siegmund, A. Mischok, K. Leo, M. Campoy-Quiles, W. Li, *Adv. Mater.* **2017**, 29, 1702184.
- [74] S. Ullbrich, B. Siegmund, A. Mischok, A. Hofacker, J. Benduhn, D. Spoltore, K. Vandewal, *J. Phys. Chem. Lett.* **2017**, 8, 5621.
- [75] M. Gibert-Roca, P. Molet, A. Mihi, M. Campoy-Quiles, *J. Mater. Chem. C* **2020**, 8, 9688.
- [76] J. H. Kim, A. Liess, M. Stolte, A. M. Krause, V. Stepanenko, C. Zhong, D. Bialas, F. Spano, F. Würthner, *Adv. Mater.* **2021**, 2100582.
- [77] U. B. Cappel, S. A. Dowland, L. X. Reynolds, S. Dimitrov, S. A. Haque, *J. Phys. Chem. Lett.* **2013**, 33, 4253.
- [78] A. Panda, C. K. Renshaw, A. Oskooi, K. Lee, S. R. Forrest, *Phys. Rev. B* **2014**, 90, 045303.
- [79] M. Eyer, J. Frisch, S. Sadofev, N. Koch, E. J. List-Kratochvil, S. Blumstengel, *J. Phys. Chem. C* **2017**, 121, 21955.
- [80] H. Li, J. L. Bredas, *Adv. Mater.* **2016**, 28, 3928.
- [81] Y. Sevinchan, P. E. Hopkinson, A. A. Bakulin, J. Herz, M. Motzkus, Y. Vaynzof, *Adv. Mater. Interfaces* **2016**, 3, 1500616.
- [82] F. Eisner, G. Foot, J. Yan, M. Azzouzi, D. G. Georgiadou, W. Y. Sit, Y. Firdaus, G. Zhang, Y. H. Lin, H. L. Yip, *Adv. Mater.* **2021**, 2104654.
- [83] N. Li, P. Mahalingavelar, J. H. Vella, D.-S. Leem, J. D. Azoulay, T. N. Ng, *Mater. Sci. Eng. R Rep.* **2021**, 146, 100643.
- [84] X. Liu, Y. Lin, Y. Liao, J. Wu, Y. Zheng, *J. Mater. Chem. C* **2018**, 6, 3499.
- [85] W. Yao, Z. Wu, E. Huang, L. Huang, A. E. London, Z. Liu, J. D. Azoulay, T. N. Ng, *ACS Appl. Electron. Mater.* **2019**, 1, 660.

- [86] X. Gong, M. Tong, Y. Xia, W. Cai, J. S. Moon, Y. Cao, G. Yu, C.-L. Shieh, B. Nilsson, A. J. Heeger, *Science* **2009**, 325, 1665.
- [87] G. Simone, M. J. Dyson, C. H. Weijtens, S. C. Meskers, R. Coehoorn, R. A. Janssen, G. H. Gelinck, *Adv. Opt. Mater.* **2020**, 8, 1901568.
- [88] G. Simone, M. J. Dyson, S. C. Meskers, R. A. Janssen, G. H. Gelinck, *Adv. Funct. Mater.* **2020**, 30, 1904205.
- [89] Z. Wu, N. Li, N. Eedugurala, J. D. Azoulay, D.-S. Leem, T. N. Ng, *npj Flex. Electron.* **2020**, 4, 1.
- [90] S. Gielen, C. Kaiser, F. Verstraeten, J. Kublitski, J. Benduhn, D. Spoltore, P. Verstappen, W. Maes, P. Meredith, A. Armin, *Adv. Mater.* **2020**, 32, 2003818.
- [91] J. Wang, H. Yao, Y. Xu, L. Ma, J. Hou, *Mater. Chem. Front.* **2021**, 5, 709.
- [92] P. Bi, S. Zhang, Z. Chen, Y. Xu, Y. Cui, T. Zhang, J. Ren, J. Qin, L. Hong, X. Hao, *Joule* **2021**, 5, 2408.
- [93] D. Qian, Z. Zheng, H. Yao, W. Tress, T. R. Hopper, S. Chen, S. Li, J. Liu, S. Chen, J. Zhang, *Nat. Mater.* **2018**, 17, 703.
- [94] Z. Wu, W. Yao, A. E. London, J. D. Azoulay, T. N. Ng, *Adv. Funct. Mater.* **2018**, 28, 1800391.
- [95] M. Azzouzi, J. Yan, T. Kirchartz, K. Liu, J. Wang, H. Wu, J. Nelson, *Phys. Rev. X* **2018**, 8, 031055.
- [96] J. Benduhn, K. Tvingstedt, F. Piersimoni, S. Ullbrich, Y. Fan, M. Tropicano, K. A. McGarry, O. Zeika, M. K. Riede, C. J. Douglas, *Nat. Energy* **2017**, 2, 1.



**Hrisheekesh Thachoth Chandran** received his Ph.D. degree in materials science and engineering from the City University of Hong Kong. He is currently a postdoctoral researcher in Prof. Gang Li's group at the Hong Kong Polytechnic University. His research interests include the investigation of performance limiting factors in organic photodiodes and the study of fundamental sub-bandgap properties of organic semiconducting materials.



**Cenqi Yan** is currently a postdoctoral research scholar in Prof. Gang Li's group in the Department of Electronic and Information Engineering, The Hong Kong Polytechnic University. Her current research focuses on organic solar cells and organic photodetectors. She received her B.S. degree in material physics from Shandong University (2013) and her Ph.D. degree in mechanics (advanced materials and mechanics) from Peking University (2018).



**Gang Li** is Sir Sze-yuen Chung Endowed Professor in renewable energy in the Department of Electronic and Information Engineering, associate director of Research Institute of Smart Energy (RISE) in the Hong Kong Polytechnic University. He obtained his B.S. degree from Wuhan University (China), M.S. and Ph.D. from Iowa State University (US), respectively. His research interests are materials, device engineering, and device physics in organic semiconductors and hybrid perovskite semiconductors, focusing on energy applications. He is a Fellow of the Royal Society of Chemistry (RSC), the International Society for Optics and Photonic (SPIE), and Optica.